European Biophysics Journal
https://doi.org/10.1007/s00249-019-01349-4

ORIGINAL ARTICLE

A study of Love wave acoustic biosensors monitoring the adhesion process of tendon stem cells (TSCs)

Huiyan Wu[1] · Hongfei Zu[1] · James H.-C. Wang[2] · Qing-Ming Wang[1]

Received: 31 August 2018 / Revised: 6 December 2018 / Accepted: 6 February 2019

Abstract

The Love wave biosensor is considered to be one of the most promising probing methods in biomedical research and diagnosis, and has been applied to detect the mechano–biological behaviour of cells attached to the surface of the device. More efforts should be devoted to basic theoretical research and relevant device performance analysis that may contribute to the further developments of Love wave sensors. In this study, a 36° *YX*-$LiTaO_3$-based Love wave sensor with a parylene-C wave guiding layer was adopted as a cell-based biosensor to monitor the adhesion process of tendon stem/progenitor cells (TSCs), a newly discovered cell type in tendons. A theoretical model is proposed to describe the Love wave propagation, in which the adherent cells are considered as a uniform viscoelastic layer. The effects of viscoelastic cell layer and wave guiding layer on the propagation velocity v and propagation loss (PL) are investigated. The numerical results indicate that adherent cell layers of different storage or loss shear modulus in certain ranges can induce pronounced and characteristic variations in v and PL, revealing the potential of Love wave sensors to provide useful quantitative measures on cellular mechanical properties. The sensor response to the adhesion of TSCs exhibits high consistency with experimental observations, which demonstrates the Love wave biosensor as a very promising sensor platform for investigating cellular activities under multiple physiological conditions.

Keywords Love wave acoustic sensor · Biosensor · Parylene-C · Cell adhesion

Introduction

It is known that every organism either consists of cells or by itself is a single cell, whether it is an animal, a plant or a microorganism (Hardin et al. 2012). Therefore, studies to understand cellular behaviour have an important role in both biological and biomedical fields, whether studying the cells themselves or interactions between cells and surrounding stimuli/environments. Cell adhesion to a substrate plays an important role in a variety of cellular activities (Hardin et al. 2012). Cell adhesion enhances cell attachment, functioning as not only structural links between the cytoskeleton and extracellular matrix (ECM), but also triggering signal pathways that direct cell functions. Cell–cell or cell–substrate adhesive interactions govern cell aggregation, polarity, and migration. In addition, such interactions can alter the differentiation of cells by changes in cell morphology, proliferation, and programmes of gene expression (Ginsberg et al. 1992). During the past decades, interest in the development of cell-based biosensors has increased considerably. A variety of devices have been developed as cell-based biosensors, and some of them have proven a great success and thus put into commercial production. The significant feature of cell-based biosensors is the use of living cells as the detected objects or the receptors to other stimuli from the surrounding environment (Wang and Liu 2010). With cells as the sensing elements, their basic physiological reactions to different external stimuli are observed, which can

✉ James H.-C. Wang
wanghc@pitt.edu

✉ Qing-Ming Wang
qiw4@pitt.edu

Huiyan Wu
huw27@pitt.edu

Hongfei Zu
hoz21@pitt.edu

[1] Department of Mechanical Engineering and Materials Science, Swanson School of Engineering, University of Pittsburgh, Pittsburgh, PA, USA

[2] Department of Orthopaedic Surgery, School of Medicine, University of Pittsburgh, Pittsburgh, PA, USA

Published online: 19 February 2019

be widely applied in drug development, quality control, and environment monitoring. Thus, as the crucial cellular behaviour that should be studied in depth, cell adhesion onto the sensing surface is also a necessary prerequisite for cell-based biosensor applications. The cell-based biosensor needs to support adherent living cells as a part of itself, creating the naturalistic environment required by living cells (Wang and Liu 2010). The physical and chemical parameters of the environment should be strictly controlled, providing 37 °C, 5% CO_2, and nutrition supply to maintain the metabolism of living cells for a long period. Furthermore, since cells are seeded and cultured on a sensing surface of metallic or ceramic materials, and not directly on standard cell culture wares such as a Petri dish, slide, or other glass or polymeric plastic dish, living cells should adhere to the surface without any limitations on their own biological functions, thus providing comparable references for their reactions in genuinely natural environments.

Currently, most studies referring to the cell adhesion process are based on the observation of cellular morphologies using optical microscopy, which is time-consuming, labour-intensive and qualitative in measurement. To achieve simple, fast monitoring, some sensor measurement methods have been developed, such as electric cell-substrate impedance sensing (ECIS) and surface plasmon resonance (SPR) sensing. ECIS is based on the electrical impedance change induced by cells attaching and spreading onto a central gold electrode, which provides quantitative information on morphologies and motions of cultured cells in real time (Giaever and Keese 1993). However, because the electrode is immersed in culture medium, adherent cells are required to restrict the current flow through the medium effectively to produce a detectable impedance change. As a result, there would be no reliable response from ECIS if seeded cells are of relatively low concentration and they cannot cover the entire electrode surface. SPR as a non-invasive optical technique can be applied to monitor certain cellular activities, but still lacks information in related structural or mechanical properties of cells.

In comparison, acoustic wave sensors have shown their advantages in real-time, quantitative measurements of cell activities. As the most widely used acoustic wave sensor, the quartz thickness shear mode (TSM) resonator has been applied in some studies on different types of cells (Li et al. 2005, 2007; Marx et al. 2005; Tan et al. 2009). A TSM resonator consists of a thin disk of AT-cut quartz with circular Au/Cr electrodes deposited on both sides. When its surface loading condition varies, for example with cells adhering on the surface, the electrically excited TSM acoustic wave propagation can change accordingly through the quartz crystal, allowing a simple, non-invasive, and quantitative method to extract the viscoelastic properties of adherent cells. More recently, the Love wave sensor has been considered as one of the most promising probing methods in biomedical research and diagnosis (Herrmann et al. 2001; Saitakis et al. 2010; Ballantine et al. 1997). Shear horizontal surface acoustic waves (SH-SAWs) can be generated by delay line inter-digital transducers (IDTs) on, for example, a 36° *YX*-$LiTaO_3$ substrate, in which the propagating waves have a shear horizontal polarization along the propagation direction. A Love wave sensor is composed of a SH–SAW device with an additional thin film layer that has a lower shear wave velocity than the substrate to guide these waves along the surface. Compared with the traditional TSM acoustic waves, Love waves display extremely high sensitivity to certain surface perturbations as well as favourable inertness to other surrounding factors, especially to the number of bonds formed within the relatively short distance of ~ 50 nm from the surface (Ballantine et al. 1997; White 1970). As the key part of a Love wave sensor, the acoustic wave guiding layer plays a crucial role in improving its sensitivity. Various thin film materials have been considered as the guiding layer, such as ZnO, SiO_2, and PMMA (Gizeli 1997; Bender et al. 2000; Kalantar-Zadeh et al. 2003). With a lack of proper biocompatible interfaces, most of the previous studies on Love wave sensors did not pay attention to their potential application in cell-based biosensing. Some relevant experimental studies have reported the use of some biocompatible polymer wave guiding layers, such as PMMA (Gizeli 1997; Bender et al. 2000), polyimide (Branch and Brozik 2004), and novolac (Gizeli et al. 2003; Matatagui et al. 2011). Parylene-C (poly(2-chloro-*p*-xylylene)) has been proven as one of the ideal wave guiding layers due to its good uniformity, compactness, and adhesion to the substrate (Lange et al. 2007). More importantly, parylene-C film possesses comparable cell and protein compatibility to the standard tissue culture substrate, indicating its great potential as a biocompatible interface for biomedical devices (Chang et al. 2007). Thus, a 36° *YX*-$LiTaO_3$-based Love wave sensor is adopted as a cell-based biosensor to monitor the cell adhesion process in this study, and parylene-C film is deposited on it as both the wave guiding layer and biocompatible interface.

Recent experimental studies have reported some cell-based applications of Love wave sensors; however, there is no mature theoretical analysis on them (Zhang et al. 2016). Most of these studies merely described the electrical sensor response to specific cellular behaviours from a perspective of experimental observation, but lacking in-depth theoretical explanation on the internal relation between signal changes and the corresponding cellular behaviours. In fact, without cellular structural or mechanical properties as intermediate parameters, this internal relation could not be established successfully. Perturbation theory, as an approximation method, was adopted in the Love wave sensor analyses and the computational results agreed well with experimental results at the initial stage. However, an increasing deviation

was found as the conditions varied continuously (Wang et al. 1994; Du et al. 1996). Based on the perturbation theory, considering the Love wave sensor as a simple mass sensor, an approximate linear relation was set up in some studies, in which no clear meaning was given to the linear relation coefficient. Along with a continuously varying condition, linear relation could not be maintained since the approximation prerequisite was not satisfied any more. So far, some studies have reported the theoretical determination of device performance parameters of Love wave sensors based on different assumptions or theoretical models, in which the resonance frequency shift or insertion loss change caused by the viscoelastic wave guiding layer and liquid medium was analyzed (Liu et al. 2013; McHale et al. 2002, 2003). Nevertheless, due to the lack of experiment-related discussion, there is little research focusing on theoretical modeling of cell-based Love wave sensors, and an in-depth, comprehensive theoretical analysis is still lacking. Currently, the transduction process of cellular output to electrical signals that can be measured and analyzed has not been fully understood in Love wave biosensors. Therefore, more efforts need be devoted for a better understanding of the relation between variations in sensor response (e.g. resonance frequency, insertion loss) and cellular properties, thus achieving quantitative characterization of adherent cells in response to physical, chemical, or biological stimulus. The performance of cell-based Love wave sensors should be investigated based on a relatively mature theoretical model, which can contribute to sensor measurements and applications.

In this study, a 36° *YX*-$LiTaO_3$-based Love wave sensor with a parylene-C wave guiding layer is adopted to monitor the adhesion process of tendon stem/progenitor cells (TSCs), a newly discovered cell type in tendons. Assuming the cells attached to the surface of the device as a uniform viscoelastic layer, a theoretical model is developed to describe the Love wave propagation in the wave guiding layer, adherent cell layer, and penetration into the liquid medium. Based on this, the effects of viscoelastic cell layer and wave guiding layer on the propagation velocity v and propagation loss PL are analyzed. The sensor response to the adhesion process of TSCs agrees well with the experimental results, which validates the theoretical model for Love wave sensor design.

Theoretical model and analytical methods

SH-SAW propagation in piezoelectric crystal substrate

Figure 1 schematically illustrates the basic structure of a Love wave biosensor in this study: the Au/Ti IDT electrodes are fabricated on the surface of piezoelectric crystal substrate and a thin layer of Au/Ti is deposited on

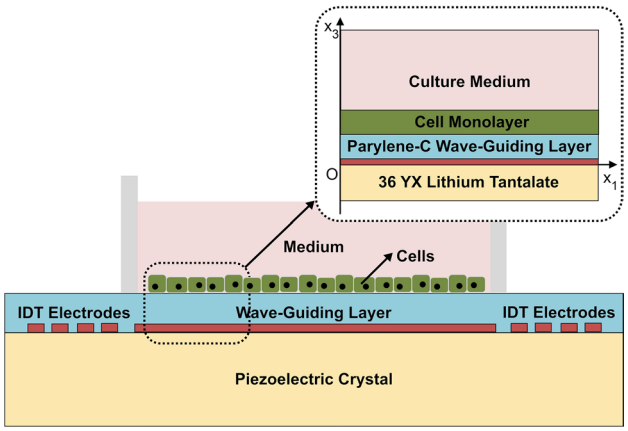

Fig. 1 Schematic structure of a cell-based Love wave biosensor

the sensing area between the input and output IDTs for metalized surface. Since the Au/Ti films are relatively thin (~ 150 nm), their effect on Love wave propagation can be neglected, thus simplifying the original theoretical model effectively. A wave-guiding layer is deposited on electrodes, and seeded cells are adhered to its surface. For analysis purpose, a 3-D Cartesian coordinate system x_1, x_2, and x_3 is established for the basic unit structure of a Love wave biosensor, where the x_1 axis is parallel to the direction of Love wave propagation, the x_2 axis is in the polarization direction, and the x_3 axis is perpendicular to the surface of the piezoelectric crystal substrate. The wave guiding layer and adherent cell layer occupy the domains of $0 \le x_3 \le h_1$ and $h_1 \le x_3 \le h_2$, respectively. Both piezoelectric crystal substrate and liquid medium are considered semi-infinite.

The constitutive equations for a piezoelectric crystal substrate are (Auld 1973):

$$\begin{aligned} T &= cS - eE, \\ D &= \varepsilon E + eS, \end{aligned} \tag{1}$$

where c, e, and ε represent the elastic, piezoelectric, and permittivity constant matrices, respectively. T and S denote the stress tensor and strain tensor, and D and E are the electric displacement and electric field intensity. With

$$S = \nabla u, \tag{2}$$

$$E = -\nabla \varphi, \tag{3}$$

where u and φ are, respectively, the particle displacement and electric potential, S and E can be eliminated from the constitutive Eq. (1). Meanwhile, neglecting gravity and other internal forces, the particle motion follows Newton's second law as:

$$\nabla \times T = \rho \frac{\partial^2 u}{\partial t^2}, \tag{4}$$

where ρ is the density of the piezoelectric crystal substrate. The divergence of the electric displacement is zero when there are no external electric charges,

$$\nabla \times D = 0. \tag{5}$$

Replacing (1) with (4), (5), the constitutive equations with respect to u and φ are rewritten as follows:

$$\begin{aligned} c_{ijkl}\frac{\partial^2 u_l}{\partial x_j \partial x_k} + e_{ijk}\frac{\partial^2 \varphi}{\partial x_j \partial x_k} &= \rho\frac{\partial^2 u_i}{\partial t^2} \\ -\varepsilon_{ij}^{S}\frac{\partial^2 \varphi}{\partial x_i \partial x_j} + e_{ijk}\frac{\partial^2 u_k}{\partial x_i \partial x_j} &= 0. \end{aligned} \tag{6}$$

In previous studies, it was shown that pure shear particle motion could be excited electrically for materials with specific elastic stiffness and piezoelectric coefficient matrices, such as quartz crystal with specific cuts (Jakoby and Vellekoop 1997; Liu and He 2010). Different from quartz crystal cuts, for 36° *YX*-$LiNbO_3$ and 36° *YX*-$LiTaO_3$ of a 3 m point group, attenuation due to leaky waves can be minimized and the predominant component of surface particle motion throughout the sensing area is shear horizontal. With x_1 axis in the direction of Love wave propagation and x_3 axis perpendicular to the surface of piezoelectric crystal substrate, the acoustic wave equations are not varied with x_2. Assuming the general solution of u and φ in piezoelectric crystal substrate as

$$\begin{aligned} u_i &= U_i \mathrm{e}^{-k\beta x_3}\mathrm{e}^{j(\omega t - kx_1)},\ i = 1,2,3, \\ \varphi &= \Phi \mathrm{e}^{-k\beta x_3}\mathrm{e}^{j(\omega t - kx_1)}, \end{aligned} \tag{7}$$

where the wave number $k = k_0 - j\alpha = \omega/\upsilon - j\alpha$ ($\alpha > 0$), υ is the propagation velocity, α is the attenuation factor of wave propagation, and α is << 1 for normal piezoelectric crystal substrates. Substituting (7) into (6), linear homogeneous equations with respect to U_1, U_2, U_3, and Φ can be obtained with a 4×4 coefficient matrix. For an effective nontrivial solution, the determinant of coefficient matrix should be zero, which results in an eighth-order polynomial equation of β. A part of the surface waves propagate along the negative direction of x_3, and when $x_3 \to -\infty$, the particle displacement u and the electric potential φ tend to vanish. Thus, (1) for complex solutions of β, roots with negative real parts are rational; (2) for pure imaginary solutions of β, roots with negative imaginary parts should be adopted. In this case, four of the eight roots of β are chosen, and the solution of u and φ is in the form:

$$\begin{aligned} u_i &= (M_1 A_{i1}\mathrm{e}^{-k\beta_1 x_3} + M_2 A_{i2}\mathrm{e}^{-k\beta_2 x_3} + M_3 A_{i3}\mathrm{e}^{-k\beta_3 x_3} \\ &\quad + M_4 A_{i4}\mathrm{e}^{-k\beta_4 x_3})\mathrm{e}^{j(\omega t - kx_1)},\quad i = 1,2,3, \\ \varphi &= (M_1 A_{41}\mathrm{e}^{-k\beta_1 x_3} + M_2 A_{42}\mathrm{e}^{-k\beta_2 x_3} + M_3 A_{43}\mathrm{e}^{-k\beta_3 x_3} \\ &\quad + M_4 A_{44}\mathrm{e}^{-k\beta_4 x_3})\mathrm{e}^{j(\omega t - kx_1)}, \end{aligned} \tag{8}$$

where $[A_{1j}, A_{2j}, A_{3j}, A_{4j}]$ is the corresponding nontrivial solution of the linear homogeneous equations with β_j ($j = 1,2,3,4$). M_{1-4} are the coefficients to be determined by boundary conditions. With the general solution into constitutive relations (1), the shear stress on the x_1–x_2 plane and the electric potential along the x_3 direction in the piezoelectric crystal substrate can be calculated as follows,

$$\begin{aligned} T_{13} &= -k(M_1 R_1 \mathrm{e}^{-k\beta_1 x_3} + M_2 R_2 \mathrm{e}^{-k\beta_2 x_3} + M_3 R_3 \mathrm{e}^{-k\beta_3 x_3} \\ &\quad + M_4 R_4 \mathrm{e}^{-k\beta_4 x_3})\mathrm{e}^{j(\omega t - kx_1)}, \\ R_i &= c_{55}\beta_i A_{1i} + jc_{56}A_{2i} + jc_{55}A_{3i} + j\mathrm{e}_{15}A_{4i},\ i = 1,2,3,4, \\ T_{23} &= -k(M_1 S_1 \mathrm{e}^{-k\beta_1 x_3} + M_2 S_2 \mathrm{e}^{-k\beta_2 x_3} + M_3 S_3 \mathrm{e}^{-k\beta_3 x_3} \\ &\quad + M_4 S_4 \mathrm{e}^{-k\beta_4 x_3})\mathrm{e}^{j(\omega t - kx_1)}, \\ S_i &= jc_{41}A_{1i} + c_{44}\beta_i A_{2i} + c_{43}\beta_i A_{3i} + \mathrm{e}_{34}\beta_i A_{4i}, \\ &\quad i = 1,2,3,4, \\ T_{33} &= -k(M_1 T_1 \mathrm{e}^{-k\beta_1 x_3} + M_2 T_2 \mathrm{e}^{-k\beta_2 x_3} + M_3 T_3 \mathrm{e}^{-k\beta_3 x_3} \\ &\quad + M_4 T_4 \mathrm{e}^{-k\beta_4 x_3})\mathrm{e}^{j(\omega t - kx_1)}, \\ T_i &= jc_{31}A_{1i} + c_{34}\beta_i A_{2i} + c_{33}\beta_i A_{3i} + \mathrm{e}_{33}\beta_i A_{4i}, \\ &\quad i = 1,2,3,4, \\ D_3 &= -k(M_1 W_1 \mathrm{e}^{-k\beta_1 x_3} + M_2 W_2 \mathrm{e}^{-k\beta_2 x_3} + M_3 W_3 \mathrm{e}^{-k\beta_3 x_3} \\ &\quad + M_4 W_4 \mathrm{e}^{-k\beta_4 x_3})\mathrm{e}^{j(\omega t - kx_1)}, \\ W_i &= j\mathrm{e}_{31}A_{1i} + \mathrm{e}_{34}\beta_i A_{2i} + \mathrm{e}_{33}\beta_i A_{3i} - \varepsilon_{33}\beta_i A_{4i}, \\ &\quad i = 1,2,3,4. \end{aligned} \tag{9}$$

Wave propagation in wave guiding layer and adherent cell layer

Compared with (6) for piezoelectric materials, constitutive equations in regard to u and φ for normal elastic and dielectric materials are in a simple form (Ballantine et al. 1997),

$$\begin{aligned} c_{ijkl}\frac{\partial^2 u_l}{\partial x_j \partial x_k} &= \left(\mu_{ijkl} + j\omega\eta_{ijkl}\right)\frac{\partial^2 u_l}{\partial x_j \partial x_k} \\ &= \mu_{ijkl}\frac{\partial^2 u_l}{\partial x_j \partial x_k} + \eta_{ijkl}\frac{\partial^2 \dot{u}_l}{\partial x_j \partial x_k} = \rho_{\mathrm{L}}\frac{\partial^2 u_i}{\partial t^2} \\ &\quad - \varepsilon_{ij}^{S}\frac{\partial^2 \varphi}{\partial x_i \partial x_j} = 0, \end{aligned} \tag{10}$$

where μ, η are the stiffness and dynamic viscosity constant, and ρ_{L} is the density. The general solution of u and φ in the wave guiding layer can be expressed as

$$\begin{aligned} u_i^{\mathrm{L}} &= U_i \mathrm{e}^{jk\beta_{\mathrm{L}i}x_3}\mathrm{e}^{j(\omega t - kx_1)},\quad i = 1,2,3, \\ \varphi^{\mathrm{L}} &= \Phi \mathrm{e}^{jk\beta_{\mathrm{L}4}x_3}\mathrm{e}^{j(\omega t - kx_1)}. \end{aligned} \tag{11}$$

For 36° *YX*-$LiTaO_3$, the predominant component of surface waves has a shear horizontal polarization along the propagation direction. To simplify our theoretical model, only particle movement along x_2 would be considered in continuous

boundary conditions. Substituting (11) into (10), u_2 and φ can be independently calculated as follows:

$$\begin{aligned} u_2^{\mathrm{L}} &= (M_5 \mathrm{e}^{jk\beta_{\mathrm{L}2}x_3} + M_6 \mathrm{e}^{-jk\beta_{\mathrm{L}2}x_3})\mathrm{e}^{j(\omega t - kx_1)}, \\ \varphi^{\mathrm{L}} &= (M_7 \mathrm{e}^{kx_3} + M_8 \mathrm{e}^{-kx_3})\mathrm{e}^{j(\omega t - kx_1)}, \end{aligned} \tag{12}$$

where

$$\beta_{\mathrm{L}2} = \left(\frac{\omega^2 \rho_{\mathrm{L}}}{k^2 c_{44}} - 1\right)^{1/2}. \tag{13}$$

and M_{5-8} are the coefficients to be determined by the boundary conditions. For an ideal elastic guiding layer ($\eta_{44}=0$), $\beta_{\mathrm{L}2}$ expression can be simplified as $\beta_{\mathrm{L}2}=(v^2\rho_{\mathrm{L}}/\mu_{44}-1)^{1/2}$. The stress on the x_1–x_2 plane along the x_2 direction in the wave guiding layer can be calculated as

$$T_{23}^{\mathrm{L}} = jk\beta_{\mathrm{L}2}c_{44}(M_5 \mathrm{e}^{jk\beta_{\mathrm{L}2}x_3} - M_6 \mathrm{e}^{-jk\beta_{\mathrm{L}2}x_3})\mathrm{e}^{j(\omega t - kx_1)}. \tag{14}$$

The Maxwell–Weichert model is introduced to describe the complex shear modulus of the viscoelastic polymer wave guiding layer. In the linear model for viscoelasticity, the relationship of shear stress and rate of strain can be described by a spring and a dashpot in series. The total rate of strain contains an elastic part and a viscous part, and a relaxation time $\tau=\eta_0/\mu_0$ can be introduced. An additional branch that only includes a spring is labeled as an elastic branch, which ensures that the material would eventually return to its original shape rather than result in plastic deformation. As a result, the expression of the shear modulus can be written as (Liu et al. 2013):

$$c_{44} = \mu_0 + \sum \mu_n \frac{i\omega\tau_n}{1 + i\omega\tau_n}. \tag{15}$$

The viscosity is very small when $\omega\tau_n$ approaches zero or infinity. In this study, this expression with $n=1$ will be used in (15).

u_2 and φ of the adherent cell layer can be solved in a similar method as follows:

$$\begin{aligned} u_2^{\mathrm{P}} &= \left(M_9 \mathrm{e}^{jk\beta_{\mathrm{P}2}(x_3-h_1)} + M_{10}\mathrm{e}^{-jk\beta_{\mathrm{P}2}(x_3-h_1)}\right)\mathrm{e}^{j(\omega t - kx_1)}, \\ \varphi^{\mathrm{P}} &= \left(M_{11} \mathrm{e}^{k(x_3-h_1)} + M_{12}\mathrm{e}^{-k(x_3-h_1)}\right)\mathrm{e}^{j(\omega t - kx_1)}, \end{aligned} \tag{16}$$

$$\beta_{\mathrm{P}2} = \left(\frac{\omega^2 \rho_{\mathrm{P}}}{k^2 c_{\mathrm{P}}} - 1\right)^{1/2}, \tag{17}$$

where h_1 is the thickness of the wave guiding layer, and ρ_{P} and c_{P} are the density and complex shear modulus of the adherent cell layer, respectively. Similarly, the stress on the x_1–x_2 plane along x_2 direction in the cell layer can be obtained as

$$T_{23}^{\mathrm{L}} = jk\beta_{\mathrm{P}2}c_{\mathrm{P}}(M_9 \mathrm{e}^{jk\beta_{\mathrm{P}2}x_3} - M_{10}\mathrm{e}^{-jk\beta_{\mathrm{P}2}x_3})\mathrm{e}^{j(\omega t - kx_1)}. \tag{18}$$

Wave penetration into the liquid medium

When a Love wave sensor is used in a liquid medium, a small amount of acoustic wave energy will propagate into the liquid medium with a decay length. To avoid unexpected effects induced by the high dielectric coefficient of liquid medium, the surface of piezoelectric crystal substrate is usually metalized, resulting in $\varphi=0$ at $x_3=0$. In this case, the velocity field generated in contacting medium by the in-plane oscillation of the wave guiding layer is determined by solving the incompressible Navier–Stokes equations (Ballantine et al. 1997):

$$\begin{aligned} &\nabla \times v = 0, \\ &\rho_{\mathrm{M}}\left(\frac{\partial v}{\partial t} + v \times \nabla v\right) = -\nabla p + \nabla \times \eta_{\mathrm{M}}\left(\nabla v + \nabla v^{\mathrm{T}}\right), \end{aligned} \tag{19}$$

where v represents the fluid velocity, ρ_{M}, η_{M} are respectively the density and dynamic viscosity of medium, and p is the pressure. When the velocity initiated by boundary perturbations is considered small, these nonlinear terms can be eliminated from (19), and the constitutive equations can be simplified as follows:

$$\begin{aligned} &\nabla \times v = 0, \\ &\rho_{\mathrm{M}}\frac{\partial v}{\partial t} = -\nabla p + \nabla \times \eta_{\mathrm{M}}\left(\nabla v + \nabla v^{\mathrm{T}}\right). \end{aligned} \tag{20}$$

Assuming the general solution of $\boldsymbol{v}$ in a liquid medium as

$$v_i^{\mathrm{M}} = U_i \mathrm{e}^{-k\beta_{\mathrm{M}i}(x_3-h)}\mathrm{e}^{j(\omega t - kx_1)}, \quad i = 1, 2, 3 \tag{21}$$

and substituting (21) into (20), v_2 can be solved independently from the momentum equation without other unknown variables involved. Correspondingly, a quadratic equation with respect to $\beta_{\mathrm{M}2}$ is obtained. Since part of the surface waves propagate along the positive direction of x_3, and when $x_3 \to \infty$, v_2 tends to zero, only $k\beta_{\mathrm{M}2}$ with positive real part can be adopted, and the solution of v_2 is as follows:

$$v_2^{\mathrm{M}} = M_9 \mathrm{e}^{-k\beta_{\mathrm{M}2}(x_3-h)}\mathrm{e}^{j(\omega t - kx_1)}, k\beta_{\mathrm{M}2} = \sqrt{k^2 + j\rho_{\mathrm{M}}\omega/\eta_{\mathrm{M}}}, \tag{22}$$

where M_9 is the coefficient to be determined by boundary conditions. The shear stress on the x_1–x_2 plane along the x_2 direction in a liquid medium is also obtained:

$$T_{23}^{\mathrm{M}} = -jk\beta_{\mathrm{M}2}\eta_{\mathrm{M}}M_9 \mathrm{e}^{-jk\beta_{\mathrm{M}2}(x_3-h)}\mathrm{e}^{j(\omega t - kx_1)}. \tag{23}$$

It is well known that for the high-viscosity liquid at high frequencies it might be necessary to consider the relaxation effect. For a cell-based Love wave biosensor, the cell culture medium is considered the low-viscosity liquid ($\eta_{\mathrm{M}} < 10$ cp), and thus only the real part of viscosity would be taken into account.

Boundary conditions of a layered love wave sensor

As shown in the previous sections, there are a series of undetermined coefficients (M_1, M_2, M_3, M_4,…) in the u, φ, and υ expressions. When a Love wave sensor with metalized surface is placed in liquid, nine coefficients ($M_{9–10}$, M_{13} in addition to $M_{1–6}$) need to be determined though nine independent boundary relations. For 36° *YX*-$LiTaO_3$, the predominant component of surface particle motion is shear horizontal. To simplify our theoretical model, only particle movement along x_2 would be considered in continuous boundary conditions. Thus, based on the continuity of displacement, stress, electric potential, and electric displacement at contact interfaces,

$$\begin{aligned}
&x_3 = 0, u_2 = u_2^{\mathrm{L}} \Rightarrow M_1A_{21} + M_2A_{22} + M_3A_{23} \\
&\quad + M_4A_{24} = M_5 + M_6, \\
&x_3 = 0, T_{23} = T_{23}^{\mathrm{L}} \Rightarrow M_1S_1 + M_2S_2 + M_3S_3 \\
&\quad + M_4S_4 = -jc_{44}\beta_{\mathrm{L}2}(M_5 - M_6), \\
&x_3 = h_1, u_2^{\mathrm{L}} = u_2^{\mathrm{P}} \Rightarrow M_5\mathrm{e}^{ik\beta_{\mathrm{L}2}h_1} + M_6\mathrm{e}^{-ik\beta_{\mathrm{L}2}h_1} \\
&\quad = M_9 + M_{10}, \\
&x_3 = h_1, T_{23}^{\mathrm{L}} = T_{23}^{\mathrm{P}} \Rightarrow c_{44}\beta_{\mathrm{L}2}(M_5e^{ik\beta_{\mathrm{L}2}h_1} - M_6\mathrm{e}^{-ik\beta_{\mathrm{L}2}h_1}) \\
&\quad = c_{\mathrm{P}}\beta_{\mathrm{P}2}(M_9 - M_{10}), \\
&x_3 = h_1 + h_2, v_2^{\mathrm{P}} = v_2^{\mathrm{M}} \Rightarrow M_9\mathrm{e}^{ik\beta_{\mathrm{P}2}h_2} + M_{10}\mathrm{e}^{-ik\beta_{\mathrm{P}2}h_2} \\
&\quad = M_{13}/i\omega, \\
&x_3 = h_1 + h_2, T_{23}^{\mathrm{P}} = T_{23}^{\mathrm{M}} \Rightarrow c_{\mathrm{P}}\beta_{\mathrm{P}2}(M_9\mathrm{e}^{ik\beta_{\mathrm{P}}h_2} \\
&\quad - M_{10}\mathrm{e}^{-ik\beta_{\mathrm{P}}h_2}) = i\beta_{\mathrm{M}}\eta_{\mathrm{M}}M_{13}, \\
&x_3 = 0, \varphi = 0 \Rightarrow M_1A_{41} + M_2A_{42} \\
&\quad + M_3A_{43} + M_4A_{44} = 0,
\end{aligned} \tag{24}$$

where h_2 is the thickness of adherent cell layer. The particle movement along the x_2 direction is dominant compared to the movements in the x_1 and x_3 directions. As a result, the additional stress boundary equations are:

$$\begin{aligned}
&x_3 = 0, T_{13} = 0 \Rightarrow M_1R_1 + M_2R_2 + M_3R_3 + M_4R_4 = 0, \\
&x_3 = 0, T_{33} = 0 \Rightarrow M_1T_1 + M_2T_2 + M_3T_3 + M_4T_4 = 0.
\end{aligned} \tag{25}$$

The combination of Eqs. (24) and (25) forms a set of linear homogeneous equations with a 9×9 coefficient matrix with respect to undetermined coefficients. Dispersion relation for the layered Love wave sensor can be obtained by evaluating the propagation velocity υ and attenuation factor α, which can satisfy the determinant of coefficient matrix to be zero. However, since particle motions along x_1, x_3 in all layers are neglected, an approximate calculation need to be performed instead, in which υ and α are determined to minimize the determinant of the coefficient matrix. A series of values of propagation velocity υ and attenuation factor α are tried until the determinant is minimized within the predetermined accuracy: for a specific thickness h of cell layer, firstly the discretization of α within a physically possible range is operated; then, for each discretized $\alpha(i)$, where i is assigned from 1 to m and m is the number of test points, the corresponding $\upsilon(i)$ is obtained by seeking the minimum point of determinant curve; with all valid solution sets ($\upsilon(i)$, $\alpha(i)$) recorded, the optimal solution is finally selected which can make the determinant function get the smallest value. Subsequently, the errors from approximation are also evaluated by comparing the particle displacements in x_1, x_2, x_3 at the interface of the $LiTaO_3$ substrate and wave guiding layer, thus proving the validity of our assumption. After the attenuation factor α is determined, the propagation loss per millimeter (mm) is given by Jakoby and Vellekoop (1997)

$$\mathrm{PL} = -0.02\alpha \log e. \tag{26}$$

Results and discussion

From the theoretical model discussed above, a series of numerical results are obtained for a 36° *YX*-$LiTaO_3$-based Love wave biosensor. The period of Au/Ti IDTs is 32 μm. A thin layer of Au/Ti is fabricated on the sensing area between the input and output IDTs, giving an operating frequency around 128 MHz. The parylene-C film is deposited on the surface of the Au/Ti films as the wave guiding layer. The elastic, piezoelectric, and permittivity constant matrices, as well as the density of $LiTaO_3$ crystal reported by Smith et al. are adopted for this work (Smith and Welsh 1971). The material parameters of the wave guiding layer are set as follows: for a pure elastic case, $\rho_{\mathrm{L}} = 1289$ kg/m^3, $c_{44} = \mu_{44} = 0.985$ GPa; and for a viscoelastic case, $\rho_{\mathrm{L}} = 1289$ kg/m^3, $\mu_0 = \mu_1 = 0.985$ GPa, $\tau = 0.01$, 0.02 ns. In the latter case, the storage shear modulus is set at a relatively constant value around $\mu_{44} = 0.985$ GPa with varying angular frequency ω, when the loss shear modulus changes in orders of magnitude by setting different relaxation times τ. In addition, with the cell culture medium as the liquid medium in the computation which has similar properties to pure water, the values of $\rho_{\mathrm{M}} = 1000$ kg/m^3 and $\eta_{\mathrm{M}} = 0.00102$ were used.

Generally speaking, the performance of the Love wave biosensors, such as resonance frequency or insertion loss, is affected by a series of factors in various degrees. Previous studies reported the effects of piezoelectric crystal substrate (Wang et al. 1994), viscoelasticity of guiding layer (Matatagui et al. 2011), and liquid medium (Gaso et al. 2013) on the insertion loss of the Love wave sensors. In our previous study, these factors were evaluated separately through a comprehensive theoretical analysis (Wu et al. 2017). When choosing the optimal thickness of the wave guiding layer, a balance is suggested among a large propagation velocity, a high coupling coefficient, a large mass

sensitivity, and a low propagation loss. For a Love wave biosensor with either an elastic wave guiding layer or a viscoelastic wave guiding layer, an optimal normalized guiding layer thickness is considered at the vicinity of $h_1/\lambda = \sim 0.05$ in vacuum, and ~ 0.048 in liquid (water). For parylene-C, the corresponding thickness should be 1.5–1.6 µm. Thus, in this study, a 36° *YX*-$LiTaO_3$-based Love wave biosensor with 1.6-µm parylene-C guiding layer is adopted for monitoring the adhesion process of TSCs.

In the meantime, from Eq. (17), the response of the Love wave sensors also strongly depends on the density and viscoelasticity of adherent cells (ρ_P, c_P). In our previous study, the quartz TSM resonator was applied to characterize the viscoelastic properties of aging and young TSCs bounded on its surface (Wu et al. 2015). TSCs were isolated from both old and young rats, and allowed to grow to confluency on the surface of TSM resonators. The admittance spectrums of TSM resonators with adherent TSCs were acquired, and a series of complex shear modulus $G' + jG''$ as well as the average thickness of TSC monolayer was calculated based on a two-layer-loading transmission line model (TLM). With the preset density of 1000 kg/m^3, the viscoelasticity of aging and young TSCs were $21608 + 136209j$ Pa and $985 + 116582j$ Pa, respectively. According to the viscoelasticity theory, complex shear modulus $c_P = G' + jG''$ is dependent on the oscillation frequency ω (Fabry et al. 2001; Smith et al. 2005). An approximation of converted viscoelasticity at a high frequency (~ 128 MHz) of $2000 + 100000j$ Pa is used for the young TSCs in this study. The G' and G'' as statistical stiffness and viscosity of the TSC monolayer can exhibit the characteristic viscoelasticity of individual TSC in a group and at the same time avoid too many fluctuations from individual differences.

After TSCs' viscoelasticity of $2000 + 100000j$ Pa is determined, the propagation velocity v and propagation loss PL for a Love wave sensor with adherent young TSCs are calculated based on the theoretical model discussed above. In both Figs. 2 and 3 (pink dot), it can be seen that as the thickness of adherent TSC layer h_2 increases, the propagation velocity v increases, and the propagation loss PL decreases. Evident changes in v and PL are observed in the early stage of an increase in cell layer thickness ($h_2 < 6$ nm). With h_2 increased further to > 10 nm, both v and PL tend to be stable without any more obvious variations. The peak value of v is obtained at $h_2 = \sim 8$ nm, leading to the maximum resonance frequency of a Love wave sensor in the adhesion process of TSCs. In addition, different variations in propagation velocity v and propagation loss PL of Love wave sensors versus the adherent cell layer thickness h_2 can be caused by adherent cells of different storage or loss shear modulus. Figure 2 shows a set of curves for the Love wave sensors with adherent cell layer of continuously varying storage modulus from 2×10^2 to 2×10^6 Pa and fixed loss modulus 1×10^5 Pa.

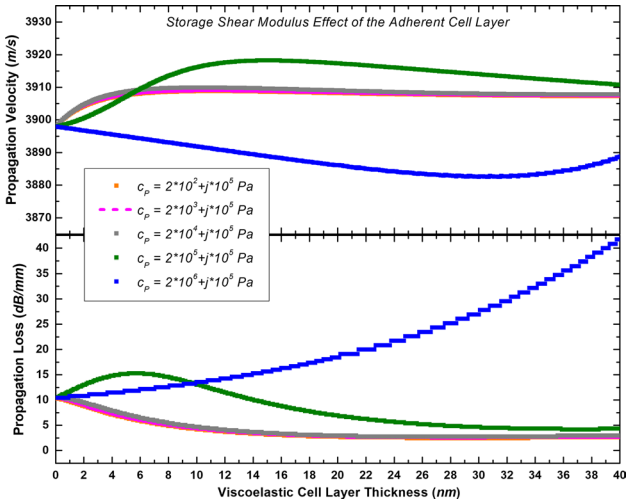

Fig. 2 Propagation velocity and propagation loss of cell-based Love wave biosensor with a 1.6-µm parylene-C wave guiding layer: with the adherent cell layer of different storage shear modulus (loss shear modulus of 10^5 Pa)

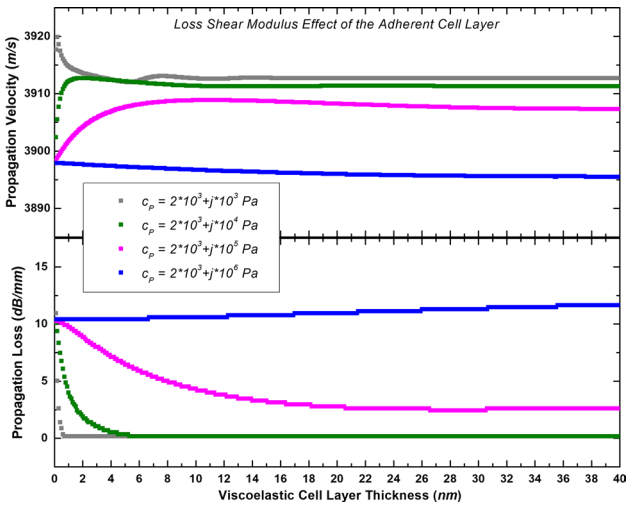

Fig. 3 Propagation velocity and propagation loss of cell-based Love wave biosensor with a 1.6-µm parylene-C wave guiding layer: with the adherent cell layer of different loss shear modulus (storage shear modulus of 2×10^3 Pa)

When the storage shear modulus of the cell layer is small ($\leq 2 \times 10^4$ Pa), the v and PL curves do not show significant differences among different modulus values. When the storage shear modulus increases further, variations in v and PL with respect to h_2 start to show different tendencies. For the case of shear modulus $G' = 2 \times 10^5$ Pa, as the adherent cell layer thickness h_2 increases, propagation velocity v increases gradually and then decreases; propagation loss PL increases slightly and then decreases dramatically. Compared with smaller storage modulus values ($G' = 2 \times 10^2$, 2×10^3, 2×10^4 Pa), its propagation velocity has a relatively large step of

increase before decreasing, leading to the initial increase of propagation loss accordingly. It might be due to spurious mode induced when the shear modulus values of the attached cell film are within a specific range. As the storage modulus of adherent cells ascends to 2×10^6 Pa, υ decreases with respect to h_2, and PL increases continuously. Figure 3 shows the curve sets of propagation velocity υ and propagation loss PL versus cell layer thickness h_2 for a cell layer of fixed storage modulus 2×10^3 Pa and continuously varying loss modulus from 1×10^3 to 1×10^6 Pa . The results indicate that under the relatively small storage shear modulus (2×10^3 Pa), adherent cells with small loss shear modulus ($\leq 1\times10^4$ Pa) cannot result in continuous, stable variations in υ and PL of the Love wave sensors: a series of weak high-order or spurious resonance peaks are observed in case of the loss modulus $G''=1\times10^3$ Pa . As the loss modulus increases further to $\geq 1\times10^5$ Pa, variations in both propagation velocity υ and propagation loss PL become stable with respect to h_2. In case of the loss modulus $G''=1\times10^6$ Pa , with the adherent cell layer thickness h_2 increases, υ decreases gradually, and PL increases. Thus, the clear, stable, characteristic variations in propagation velocity υ and propagation loss PL of Love wave sensors can be observed when the storage and loss shear modulus of the adherent cell layer are in an appropriate range. The numerical results demonstrate the potential of Love wave sensors in providing useful quantitative measures on cellular viscoelasticity during the adhesion process, indicating an advisable method for real-time monitoring of the structural and mechanical properties of adherent cells under multiple physiological conditions.

In Figs. 2 and 3, an optimal thickness of 1.6 μm is adopted for parylene-C wave guiding layer. Figure 4 shows the response of Love wave sensors with parylene-C wave guiding layers of various thicknesses in the adhesion process of TSCs. Considering the parylene-C wave guiding layer as a pure elastic layer, it can be seen that both the normalized propagation velocity change $[(\upsilon-\upsilon_0)/\upsilon_0\times100\%]$ and propagation loss PL versus the cell layer thickness h_2 exhibit similar variation tendencies for the guiding layers of different thicknesses, though the variation ranges and magnitudes are different. As h_2 increases firstly, the propagation velocity υ increases gradually and propagation loss PL decreases; as h_2 increases further, both υ and PL tend to be stable. The results from our previous study indicate that for a Love wave sensor applied in a liquid medium, with the guiding layer thickness increases, the characteristic propagation velocity υ decreases and propagation loss PL increases. Similarly, for the starting points of all curves: in the beginning, with the parylene-C layer thickness increases (≤ 1.0 μm), υ decreases slightly and its value is still >4000 m/s, and PL remains <2 dB/mm; as the thickness increases further to ≥ 1.5 μm, υ decreases dramatically to <4000 m/s and PL increases to >5 dB/mm. In addition, when the parylene-C layer is relatively

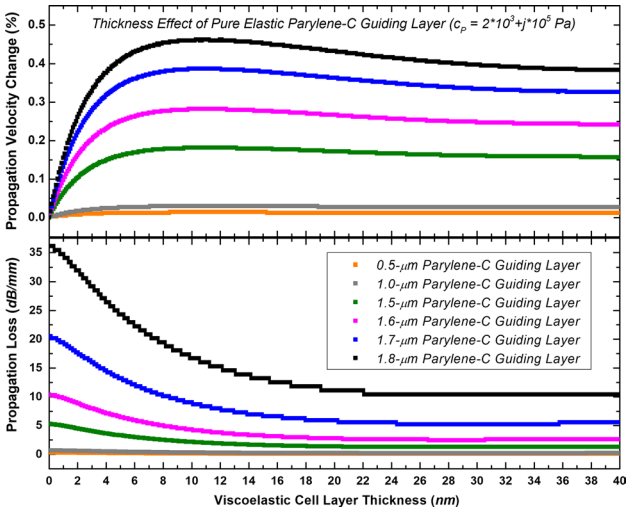

Fig. 4 Normalized propagation velocity variation and propagation loss of cell-based Love wave biosensor with a pure elastic parylene-C wave guiding layer of different thicknesses ($c_P=2\times10^3+j\times10^5$ Pa)

thin (≤ 1.0 μm), the propagation velocity υ and propagation loss PL do not show any evident change with respect to the adherent cell layer thickness h_2. Until the parylene-C layer thickness increases to ≥ 1.5 μm, with an increase in h_2, υ increases and PL decreases dramatically. Even though with different variation ranges and magnitudes, it is important to note that for the adherent TSC layer of $2000+100000j$ Pa, both sets of υ and PL curves enter a plateau, as the cell layer thickness h_2 is >20 nm. 20 nm is quite a small thickness, which can be attributed to the significant attenuation of Love waves in the viscoelastic cell layer. From this perspective, when applying the Love wave sensor to monitor the adhesion process of TSCs, the sensor response will be primarily induced by the initial interaction between attached cells and the substrate during the early stage of adherent cell layer formation.

In the discussions above, the parylene-C wave guiding layer is considered as a pure elastic layer. However, as a viscoelastic polymer, the viscous effect of parylene-C layer should be taken into account as well. As shown in Fig. 5, for an elastic wave guiding layer and a viscoelastic wave guiding layer, both the propagation velocity υ and propagation loss PL show quite similar variation tendencies versus the adherent cell layer thickness h_2. As the relaxation time τ increases from 0 (for the pure elastic case) to 0.02 ns, the curve of the propagation velocity υ shifts to a higher velocity range, and propagation loss PL moves to a larger loss zone, leading to an increase in both resonance frequency and insertion loss of Love wave sensors. The results indicate that for a Love wave sensor with the wave guiding layer of certain thickness, the viscosity of guiding layer only has limited influence in the change range of υ and PL, but not their variation tendency,

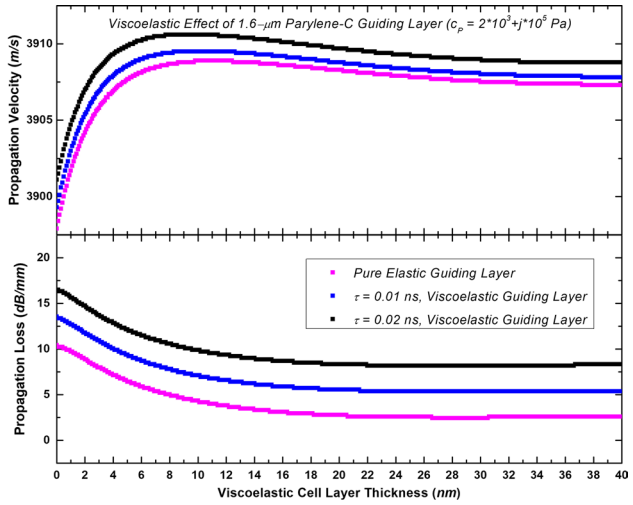

Fig. 5 Propagation velocity and propagation loss of cell-based Love wave biosensor with 1.6-μm pure elastic and viscoelastic parylene-C wave guiding layers ($c_P = 2\times10^3 + j\times10^5$ Pa)

which is quite similar with the effects of a certain wave guiding layer of varied thicknesses.

We also used the 36° *YX*-$LiTaO_3$-based Love wave sensors to monitor the adhesion process of TSCs isolated from young rats (Wu 2015). Parylene-C film as the wave guiding layer was deposited on Au/Ti electrodes by thermal deposition system. The average thickness of parylene-C film was 1.6 μm, which provides a good combination of a high mass sensitivity and a low energy loss. One rectangular tube (10 mm/16.0 mm × 12 mm) of poly(dimethylsiloxane) (PDMS, Dow Corning, Midland, MI, USA) was located around the sensing area, forming the well-like structure for TSC culture. The S_{21} loss curves were obtained by an Agilent N5230A PNA Network Analyzer (Agilent Technologies, Palo Alto, CA, USA), and an Agilent 34970A switch/control unit was series connected for converting among different sensors. Before the real-time measurement, Love wave sensors with empty wells were firstly exposed to UV light overnight to sterilize. Subsequently, 400 μl 100 μg/ml collagen type I (Stemcell Technologies, Vancouver, BC, Canada) in phosphate-buffered saline (PBS, Mediatech Inc., Manassas, VA, USA) was added into each well and kept for 2 h to cover the entire well bottom with collagen, as commonly conducted in tissue culture. After removing the collagen/PBS solution and washing these wells with PBS for three times, 400 μl TSC suspensions of different concentrations (0.5×10^5, 1.0×10^5, 2.0×10^5, 4.0×10^5 cell/ml) were added. Love wave sensors with cell suspensions were maintained in an incubator at 37 °C with 5% CO_2 for 10 h, and the corresponding S_{21} loss curves were acquired every 1 min. Meanwhile, the S_{21} loss curves of Love wave sensors with pure culture medium were also recorded as the background signal. In parallel experiments, 100 μl TSC suspensions of

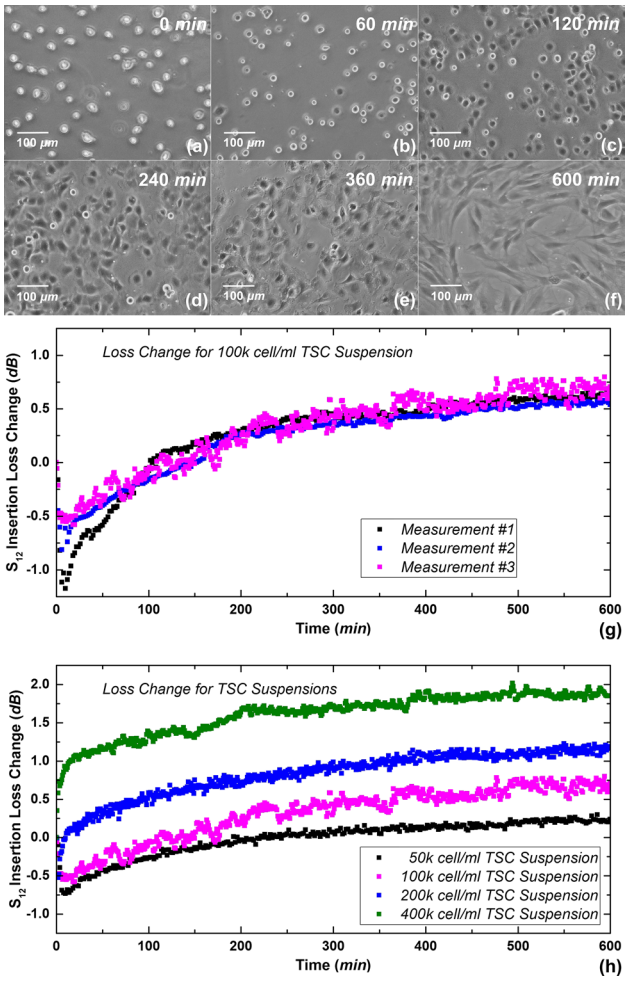

Fig. 6 Monitoring the adhesion process of TSCs: **a**–**f** Phase-contrast microscopy photos of TSCs (1×10^5 cell/ml) at different time points (**g**). Normalized loss change of Love wave sensors with addition of TSC suspensions (1×10^5 cell/ml). **h** Normalized loss change of Love wave sensors with addition of TSC suspensions with varied concentrations

identical concentrations were cultured in collagen-coated 96-well culture plate (the cell number per unit area in culture plate was designed to be the same as in the Love wave sensors) and observed by an optical microscopy (Eclipse TS100, Nikon, Japan) at a series of time points (0, 1, 2, 4, 6, 10 h).

Figure 6(a–f) are the microscopy photos of TSCs at a series of time points after 100 μl cell suspensions of 1.0×10^5 cell/ml were added into the 96-well culture plate, and (a–f) were taken after 0, 1, 2, 4, 6 and 10 h in order, respectively. The TSCs suspending in culture medium possessed a relatively spherical shape as shown in (a). When added into wells, TSCs began to go down and landed on the substrate. After 1 h, as shown in (b), half of the suspending TSCs had attached to the substrate (spherical ones with bright edges) and quite a few of them began to spread (flat black ones).

After 2 h, over 80% TSCs had attached to the substrate and began to spread [(c)]. When the incubation exceeded 4 h, over 95% TSCs had settled down on the substrate [(d))]. For attached TSCs, the first change that can be recognized was a transformation from a spherical to a flat discoid shape. Then, with these cells spreading onto the surface, significant morphological changes occurred. Through 4 h incubation, a preliminary enlarged, polygonal cell shape was observed from part of the TSCs. With continued incubation, TSCs kept spreading and formed focal adhesions (Hardin et al. 2012). The morphology variation process was almost completed after 10 h. It can be seen from (f) that all adherent TSCs possessed a characteristic elongated shape, exhibiting their high consistency and uniformity. Figure 6g illustrates the electrical response of Love wave sensors during the TSC adhesion process (1.0×10^5 cell/ml). In our experiments, insertion loss of a typical blank Love wave sensor was ~ 25 dB and decreased sharply to ~ 30 dB when pure culture media or cell suspensions were added (Wu 2015). As the incubation time increased to 10 h, insertion loss for media decreased 1 ~ 2 dB smoothly, and the insertion loss change due to TSC adhesion could be extracted accordingly from the differences between the S_{21} spectrum sets with cell suspensions and pure culture medium. As shown in Fig. 6g, the insertion loss change curves of three trials showed similar tendencies: in the first 4 h incubation, the insertion loss change caused by cell adhesion increased dramatically, and with continued incubation these curves tended to be stable. The S_{21} loss changes related well to the corresponding morphology variations of TSCs shown in (a–f). During the initial 4 *h* incubation, due to the extensive formation of integrin–ECM protein bonds between attached cells and the substrate, there was a rapid increase in the insertion loss change (Hardin et al. 2012). With continued incubation, over 95% TSCs had attached to the substrate, and the adherent cell layer was formed initially. The small portion of remaining cells was then attaching to the surface, and attached ones were spreading to occupy more surface of the substrate, thus causing a continuous smooth increase in the loss curves. In addition, the focal adhesion formation and cytoskeleton reorganization resulted in changes in the viscoelasticity of adherent cells, which might also lead to a slight increase in the insertion loss change. Once the adhesion process of TSCs was complete, the insertion loss change was inclined to be stable. Since the evident variations in the insertion loss change curves were observed in the initial 4 h incubation, it was indicated that the dominant factor of S_{21} insertion loss change was the interactions occurring in TSC attachment, the initial formation stage of the adherent TSC layer. When over 95% TSCs had attached to the substrate and integrin–ECM protein bonds had formed, the loss change curve entered a plateau gradually. Figure 6h shows the normalized loss change curves of Love wave sensors with TSC suspensions of various concentrations (0.5×10^5, 1.0×10^5, 2.0×10^5, 4.0×10^5 cell/ml). It can be seen that S_{21} loss changes presented rather similar variation tendencies for different concentrations: there was a fast increase in all of the S_{21} loss change curves in the beginning; along with continued incubation, the increase rate decreased to zero gradually, and S_{21} loss change tended to be stable. The main differences among different concentrations are merely on the duration of fast growth, as well as the magnitude of loss variation. For TSC concentrations of 0.5×10^5, 1.0×10^5 cell/ml, the fast growth lasted approximately 4 h. As the concentration increased to 2.0×10^5, 4.0×10^5 cell/ml, the fast-growing region was decreased to about 2 h and 1 h, respectively. At the same time, their growth rate in this period was significantly increased compared with that of low concentrations. This might be attributed to the increased bonds forming when TSCs were attaching to the substrate. As shown in Fig. 6d, for 1.0×10^5 cell/ml, the TSCs had not formed a uniform cell monolayer when cell spreading just began, and a considerable proportion of substrate was available for cell attachment. Therefore, in case of high concentrations, a larger number of TSCs could form integrin–ECM protein bonds at the beginning. However, when some TSCs began to spread, there was limited space for other suspended TSCs to attach, which resulted in a higher increase rate and an earlier end of fast growing. All S_{21} loss change curves can be found to go into a plateau at almost the same time. The final value of loss change increased as the concentration of TSC suspension increased. As discussed above, due to a higher TSC concentration, more TSCs would attach to the substrate in the first few of hours of incubation. With incubation, even though spreading of cells would be limited by each other to some extent and cell multilayer structure would form, the final number of adherent TSCs per unit area was still increased.

The numerical sensor response to the TSC adhesion process agrees well with our experimental observations. For a Love wave sensor in experiments, the insertion loss is determined by the wave propagation loss in the acoustic wave pathway, as well as the conversion loss during the electro-acoustic energy inter-conversion in the input and output IDTs, which is determined by the electromechanical coupling coefficient K^2 and the structure of the IDTs. With the structural design of the Love wave sensor as determined, the insertion loss change is primarily caused by the propagation loss variations occurring in the acoustic wave pathway due to cell adhesion. In numerical simulations above, attached films with the specific viscoelastic properties could induce similar variations in the insertion loss of Love wave sensors: when the thickness of adherent cell layer h_2 increases, the propagation loss PL decreases gradually. Furthermore, because of a short decay length of Love waves in liquid, in computation, when h_2 increases further to > 10 nm, PL tends to be stable. The initial formation of the adherent cell layer can result in a reduction in propagation loss PL;

in the measurements, correspondingly, the insertion loss change of the Love wave sensor increased dramatically in the early stage of cell adhesion due to the formation of integrin–ECM protein bonds. As the initial attachment of cells was complete, there was no more significant change in the loss curves. On the other hand, it should be noted that there is still a quantitative difference in the insertion loss values between theoretical calculation and experimental measurement. The typical insertion loss of a Love wave sensor in liquid in our experiments was only around 30 dB, as a sum of both energy inter-conversion loss and propagation loss. The main reason for the difference might be the variations on the stiffness of parylene-C wave guiding layer under an increasing resonance frequency. Along with the operation frequency increase, the stiffness of parylene-C films rises accordingly, leading to a relatively small insertion loss through the wave guiding layer of the same thickness. It is found that if the stiffness of parylene-C films is increased by one order of magnitude, the total propagation loss could fall down to 1/35 of the original value. Alternatively, an increase in the wave guiding layer's stiffness results in a similar consequence as the thickness reduction as Fig. 4 shows. Thus, both the starting insertion loss and loss change due to cell adhesion of the Love wave sensor were decreased in our experiments compared with the theoretical calculations. In addition, the smaller value of insertion loss change was also affected by the coverage ratio of cells on the surface of the Love wave sensor. TSCs could not form an isotropic, uniform layer on the entire sensing pathway as in the theoretical assumptions, but only partially cover the sensing area.

In comparison, the adhesion process of TSCs was also monitored by TSM resonators. Admittance spectrums of TSM resonators with TSC suspensions were acquired, and the corresponding resonance frequencies were extracted from them (Wu et al. 2015). In the beginning, as a great number of TSCs fell down and attached to the electrodes, the resonance frequency shift decreased sharply. With more and more TSCs finishing attachment, starting to spread, and forming focal adhesions, the viscoelasticity of the attached cells changed accordingly, and the resonance frequency shift of the TSM resonators increased and then decreased again. Compared with the TSM resonators, the trigger of Love wave sensor response was primarily limited to the formation of bonds between the TSCs and the substrate. Attributed to a larger decay distance of acoustic wave penetration into the liquid medium, the response of TSM resonators may be affected by more unexpected surrounding factors. The Love wave sensor exhibits high sensitivity to surface perturbations, especially bonds formed within the relatively short distance from the surface, indicating their potential for investigating subtle interactions between cell membranes and substrates involved in a variety of cellular activities.

Conclusions

In this study, a 36° *YX*-$LiTaO_3$-based Love wave sensor with a parylene-C wave guiding layer is adopted as a cell-based biosensor to monitor the adhesion process of TSCs, a kind of cell newly discovered in tendons. A theoretical model is proposed in which the cells attached to the surface of the device are considered as a viscoelastic layer. The Love wave propagation in different layers, including the wave guiding layer, adherent cell layer, and liquid medium are described. The effects of viscoelastic cell layer and wave guiding layer on both the propagation velocity v and propagation loss PL are investigated. The numerical results indicate that the adherent cells of different storage or loss shear modulus in certain ranges can induce pronounced and characteristic variations in v and PL, revealing the potential of Love wave sensors to provide useful quantitative measures on cellular mechanical properties. In comparison, the thickness and viscosity of the parylene-C wave guiding layer have limited influence on the changes of v and PL of Love wave sensors. The sensor response to the adhesion process of TSCs exhibits high consistency with the experimental observations, providing a recommended method to investigate a series of cellular activities. Based on it, the theoretical model proposed in this work is validated further for designing a Love wave biosensor, which can contribute to Love wave sensor applications.

Acknowledgements Huiyan Wu thanks Dr. J. Zhang, Dr. T. Yuan, Dr. Y. Zhou, and Dr. G. Zhao for their help during the course of this study. This work is supported in part by the NIH Grant AR060920 and AR061395 (JHW).

References

Auld BA (1973) Acoustic fields and waves in solids. Wiley, Hoboken

Ballantine DS et al (1997) Acoustic wave sensor: theory, design, and physico-chemical applications. In: Stern R, Levy M (eds) Applications of modern acoustics. Academic Press, Cambridge

Bender F, Cernosek RW, Josse F (2000) Love-wave biosensors using cross-linked polymer waveguides on LiTaO3. Electron Lett 36(19):1672–1673

Branch DW, Brozik SM (2004) Low-level detection of a *Bacillus anthracis* simulant using love-wave biosensors on 36°YX LiTaO3. Biosens Bioelectron 19(8):849–959

Chang TY et al (2007) Cell and protein compatibility of parylene-C. Langmuir 23:11718–11725

Du J et al (1996) A study of love-wave acoustic sensors. Sens Actuators A 56:211–219

Fabry B et al (2001) Scaling the microrheology of living cells. Phys Rev Lett 87(14):148102-1–148102-4

Gaso MIR et al (2013) Love wave biosensors: a review. In: Rinken T (ed) State of the art in biosensors-general aspects. InTech, London, p 360

Giaever I, Keese CR (1993) A morphological biosensor for mammalian cells. Nature 366:591–592
Ginsberg MH, Du X, Plow EF (1992) Inside-out integrin signalling. Curr Opin Cell Biol 4:766–771
Gizeli E (1997) Design considerations for the acoustic waveguide biosensor. Smart Mater Struct 6:700–706
Gizeli E et al (2003) Sensitivity of the acoustic waveguide biosensor to protein binding as a function of the waveguide properties. Biosens Bioelectron 18:1399–1406
Hardin J, Bertoni G, Kleinsmith LJ (2012) Becker's world of the cell. Pearson Education, London
Herrmann F et al (2001) Microacoustic sensors for liquid monitoring. Sens Update 9(1):105–160
Jakoby B, Vellekoop MJ (1997) Properties of love waves-applications in sensors. Smart Mater Struct 6:668–679
Kalantar-Zadeh K et al (2003) Novel love mode surface acoustic wave based immunosensors. Sens Actuators B 91:143–147
Lange K, Grimm S, Rapp M (2007) Chemical modification of parylene C coatings for SAW biosensors. Sens Actuators B 125:441–446
Li J et al (2005) Monitoring of integrin-mediated adhesion of human ovarian cancer cells to model protein surfaces by quartz crystal resonators-evaluation in the impedance analysis mode. Biosens Bioelectron 20:1333–1340
Li F, Wang JH-C, Wang Q-M (2007) Monitoring cell adhesion by using thickness shear mode acoustic wave sensors. Biosens Bioelectron 23:42–50
Liu J, He S (2010) Theoretical analysis on love waves in a layered structure with a piezoelectric substate and multiple elastic layers. J Appl Phys 107:073511-1–073511-8
Liu J et al (2013) Properties of Love Waves in a Piezoelectric Layered Structure with a Viscoelastic Guiding Layer. Smart Mater Struct 22:125034-1–125034-8
Marx KA et al (2005) Quartz crystal microbalance biosensor study of endothelial cells and their extracellular matrix following cell removal-evidence for transient cellular stress and viscoelastic changes during detachment and the elastic behavior of the pure matrix. Anal Biochem 343:23–34
Matatagui D et al (2011) Array of love-wave sensors based on quartz/novolac to detect CWA simulants. Talanta 85:1442–1447
McHale G, Newton MI, Martin F (2002) Theoretical mass sensitivity of love wave and layer guided acoustic plate mode sensors. J Appl Phys 91(12):9701–9710
McHale G, Newton ML, Martin F (2003) Theoretical mass, liquid, and polymer sensitivity of acoustic wave sensors with viscoelastic guiding layers. J Appl Phys 93(1):675–690
Saitakis M, Tsortos A, Gizeli E (2010) Probing the interaction of a membrane receptor with a surface-attached ligand using whole cells on acoustic biosensors. Biosens Bioelectron 25:1688–1693
Smith RT, Welsh FS (1971) Temperature dependence of the elastic, piezoelectric, and dielectric constants of lithium tantalate and lithium niobate. J Appl Phys 42:2219–2230
Smith BA et al (2005) Probing the viscoelastic behavior of cultured airway smooth muscle cells with atomic force microscopy: stiffening induced by contractile agonist. Biophys J 88(4):2994–3007
Tan L et al (2009) Dynamic measurement of the surface stress induced by the attachment and growth of cells on au electrode with a quartz crystal microbalance. Biosens Bioelectron 24:1603–1609
Wang P, Liu Q (2010) Cell-based biosensors: principles and applications. Artech House, Norwoord, p 271
Wang Z, Cheeke JDN, Jen CK (1994) Sensitivity analysis for love mode acoustic gravimetric sensors. Appl Phys Lett 64:2940–2942
White RM (1970) Surface elastic waves. Proc IEEE 58(8):1238–1276
Wu H et al (2015) Monitoring the adhesion process of tendon stem cells using shear-horizontal surface acoustic wave sensors. In: 2015 Joint conference of ieee international frequency control & european frequency and time forum, 2015, Denver, CO, USA
Wu H et al (2015) Aging-related viscoelasticity variation of tendon stem cells (TSC) characterized by quartz thickness shear mode (TSM) resonators. Sens Actuators B 210:369–380
Wu H et al (2017) Theoretical analysis of love wave biosensors in liquid with a viscoelastic wave guiding layer. J Appl Phys 121:054501
Zhang X et al (2016) A novel sensitive cell-based love wave biosensor for marine toxin detection. Biosens Bioelectron 77:573–579